

INFLUENCE OF CALCINATION TEMPERATURE ON THE STRUCTURAL AND PHOTOCHROMIC PROPERTIES OF NANOCRYSTALLINE MoO₃

P.JITTIARPORN^{a,c}, L.SIKONG^{a,c*}, K.KOOPTARNOND^{a,c}, W.TAWEEPREDAB^b

^a*Department of Mining and Materials Engineering, Faculty of Engineering, Prince of Songkla University, Hat Yai, Songkhla 90112, Thailand*

^b*Department of Materials Science and Technology, Faculty of Science, Prince of Songkla University, Hat Yai, Songkhla 90112, Thailand*

^c*Center of Excellence in Materials Engineering (CEME), Prince of Songkla University, Hat Yai, Songkhla, 90112, Thailand*

Nanocrystalline metastable hexagonal and thermodynamically stable orthorhombic MoO₃ were successfully synthesized by precipitation, and calcined at various temperatures in the range 200-500°C. The influence of calcination temperature on crystal structure, crystallite size, thermal properties, morphology, optical properties, and photochromic properties was determined. The 432°C phase transformation temperature of hexagonal flower-like MoO₃ to an orthorhombic platelet structure was determined. The band gap energy of MoO₃ varied from 3.13 to 3.20 eV, depending on calcination temperature. The photochromic properties were determined with UV irradiation and CIE Lab colour system. The hexagonal MoO₃ from low temperature calcination had an about seven-fold photochromic efficiency relative to orthorhombic MoO₃.

(Received September 17, 2015; Accepted November 1, 2015)

Keywords: Hexagonal MoO₃; Orthorhombic MoO₃; Precipitation method; Calcination temperature; Photochromic properties

1. Introduction

Molybdenum trioxide (MoO₃) is an important material with extensive applications in many fields such as supported catalysts, gas sensors, electrodes of rechargeable batteries, counter electrodes of dye sensitized solar cells, antimicrobials [1-5], and especially as chromogenic materials. Its electrochromic, thermochromic, and photochromic responses are defined as colour responses to the transfer of electrons by oxidation/reduction, to changes in temperature, or to electromagnetic radiation [6,7]. Applications in automobile and building glazing, and energy conservation use photochromic materials. So far, the various methods used to fabricate MoO₃ include hydrothermal, sonochemistry, sol-gel, RF magnetron sputtering, spray pyrolysis, chemical vapor deposition, precipitation, and thermal evaporation, among others [8-15].

The oxide MoO₃ has three common crystal structures. The well-known thermodynamically stable orthorhombic MoO₃ (α -MoO₃) has MoO₆ octahedral base in its unit cell, and all the MoO₃ components share edges and corners forming a zigzag chain and layered structure. The metastable monoclinic MoO₃ (β -MoO₃) has the MoO₆ octahedral unit with shared corners resulting in a distorted cube [16], and the metastable hexagonal MoO₃ (h-MoO₃) is also constructed of zigzag chains of MoO₆ octahedra connected at *cis*-positions [17]. Metastable structures often provide new and improved properties relative to thermodynamically stable structures [18].

A multitude of factors affect the photochromic efficiency of MoO₃, for example absorption of water or moisture in air [15], specific surface area of MoO₃ [8], band gap energy [8], effects of

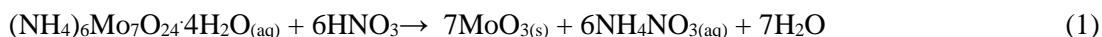
* Corresponding author: lek.s@psu.ac.th

dopants [19, 20] and oxygen vacancies or defect concentrations in the MoO₃ lattice [15]. The structure of MoO₃ may have a large effect on its photochromic properties, and it can be easily modified by a heat treatment or calcination at a high temperature. In this present work, we have investigated the effects of calcination temperature on structural, morphological, and optical properties of nanocrystalline MoO₃ powders, and we also report on the photochromic properties of particles synthesized by precipitation and calcined at temperatures in the range 200-500°C.

2. Material and methods

2.1 Synthesis of nanocrystalline MoO₃ powders

Ammonium heptamolybdate tetrahydrate ((NH₄)₆Mo₇O₂₄·4H₂O or AHM, Ajax Finechem) and concentrated nitric acid (37% HNO₃, J.T.Baker) analytical grade reagents were used as the starting materials to prepare MoO₃ powder using precipitation. First, (NH₄)₆Mo₇O₂₄·4H₂O was dissolved in distilled water to 0.2 M solution under vigorous magnetic stirring for about 15 min. Then concentrated HNO₃ was added dropwise into the AHM aqueous solution with continuous stirring. The suspension was held at 85 °C for 1 h. After that, the precipitate was collected by filtration and washed several times with distilled water and ethanol. The powder was dried at 70°C for 6 h in a hot air oven. Finally, the powder was calcined at various temperatures, namely at 200, 300, 400 and 500°C, for 1 h. The chemical reaction forming the precipitated MoO₃ is:



2.2 Characterizations

The crystalline structure and the crystallite size of the powders were characterized by X-ray diffraction (XRD, Philips X-pert) with Cu-K α radiation. The microstructures and particle sizes of the MoO₃ powders were assessed by scanning electron microscopy (SEM, Quanta, FEI). The oxidation state and functional groups of each sample were determined by X-ray photoelectron spectrometer (XPS) and Fourier transform infrared spectroscopy (FTIR, Bruker Vertex) at Synchrotron Light Research Institute (SLRI) of Thailand, respectively. Thermogravimetric analysis (TGA, PERKIN ELMER, TGA7) and differential thermal analysis (DTA, PERKIN ELMER, DTA7) were used in the range from room temperature to 800°C with a rate of 10°C/min, in nitrogen atmosphere. The optical properties of the samples were studied by recording the diffuse reflectance spectra using a UV-visible spectrophotometer (Shimadzu UV2401) and a barium sulfate (BaSO₄) plate was used as the reference.

2.3 Photochromic property testing

Photochromic properties of the powder samples were quantified by a colour difference meter (HunterLab, ColourFlex). The colour standard used was the CIE Lab uniform colour. The colour determinations of samples were done after UV irradiation at 90 W power in a reflecting box, for designated times in the range from 0 to 360 minutes. Non-irradiated MoO₃ powder was used for the white calibration reference. The L*, a* and b* colour parameters were recorded, and from them the colour differences were calculated as:

$$\Delta C = [(\Delta L^*)^2 + (\Delta a^*)^2 + (\Delta b^*)^2]^{1/2} \quad (2)$$

where ΔC is colour difference of a powder sample before and after UV irradiation, L* is the transparency index (light to dark axis), and a* and b* are the chroma indexes for green to red axis and yellow to blue axis, respectively.

3. Results and Discussion

3.1 XRD analysis

The structural and lattice parameters of MoO₃ samples were characterized using XRD. Fig.1 and Table 1 show the XRD results for the MoO₃ samples calcined at 200, 300, 400 and 500°C. For the hexagonal and orthorhombic structures of MoO₃, the lattice parameters *a*, *b* and *c* were calculated from the interplanar spacing of the {*h k l*} plane with Miller indices *h k l*. Eq. (3) is for hexagonal structure and (4) is for orthorhombic structure.

$$\frac{1}{d_{hkl}^2} = \frac{4}{3} \left[\frac{h^2 + hk + k^2}{a^2} \right] + \frac{l^2}{c^2} \quad (3)$$

$$\frac{1}{d_{hkl}^2} = \frac{h^2}{a^2} + \frac{k^2}{b^2} + \frac{l^2}{c^2} \quad (4)$$

where *d_{hkl}* is the lattice spacing of the (*hkl*) plane and *a*, *b* and *c* are the lattice parameters.

The diffraction peaks of the calcined MoO₃ samples at 200-300°C were matched to single phase hexagonal MoO₃ (JCPDS Card No.21-0569, h-MoO₃). The sharp and high intensity diffraction peaks observed indicate that the h-MoO₃ in the samples was of high crystallinity and purity. For MoO₃ calcined at 400°C, the XRD patterns indicated two structures of MoO₃ that match the h-MoO₃ (JCPDS Card No.21-0569), and the orthorhombic structure of MoO₃ (JCPDS Card No. 35-0609, α-MoO₃). The fractions of hexagonal and orthorhombic phases in the samples were 87.34% and 12.66%, respectively.

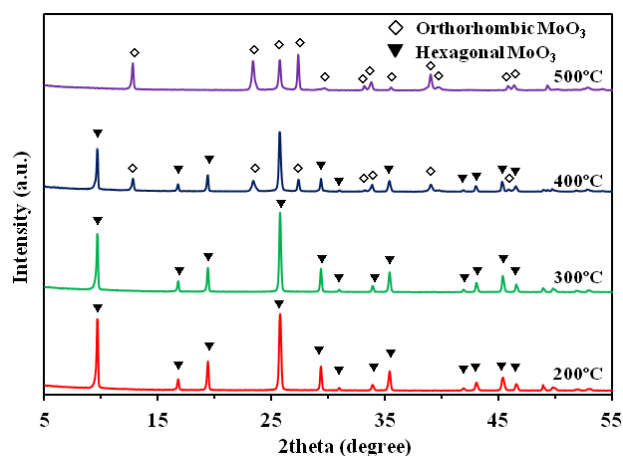


Fig.1 XRD patterns of nanocrystalline MoO₃ samples calcined at various temperatures.

With calcination temperature increased to 500°C, the diffraction peaks of single-phase orthorhombic MoO₃ appeared in the XRD patterns, and the diffraction patterns are well consistent with the JCPDS Card No.35-0609. In the XRD patterns across all samples, no characteristic peaks for other impurities were observed.

The lattice parameters of the MoO₃ powders calcined at various temperatures are summarized in Table 1. The determined lattice parameters *a* and *b* of the hexagonal MoO₃ clearly increased while *c* decreased with temperature, in the range from 200°C to 400°C. Furthermore, the lattice parameters *a*, *b* and *c* of orthorhombic MoO₃ also increased with calcination temperature, at the experimental points 400 and 500°C where it was present. The crystallite sizes of calcined MoO₃ samples can be estimated using Scherrer's formula [12].

The crystallite sizes for h-MoO₃ were estimated to be 45, 48, and 48 nm for the calcination temperatures 200, 300 and 400°C, respectively. Moreover, the crystallite sizes of α-MoO₃ were 43

and 46 nm in the samples calcined at 400 and 500°C, respectively. Increasing the calcination temperature promotes crystal grain growth and reduces defects in the crystallites [21]. A decrease in MoO₃ crystallinity decreases the grain boundary energy and the total energy of the system. In addition, the grain size as a function of time can be approximated by [22]:

$$(r)^n - (r_0)^n = Kt \quad (5)$$

where r_0 is an initial grains radius, r is the grain radius at time (t), and n is a grain-growth exponent depending on the growth mechanism. The constant K can be estimated from an Arrhenius's equation [22]:

$$K = K_0 \exp(-Q_G/RT) \quad (6)$$

where K_0 is a constant, Q_G is the activation energy of grain growth, R is the gas constant, and T is the absolute temperature. Based on Eq. (5) and (6), the crystallite size of MoO₃ should increase with calcination temperature. The calcination temperature in general tends to affect the crystallite size of a material [21].

Table 1 The crystallite structure data and optical properties of nanocrystalline MoO₃ calcined at various temperatures

Calcination temperature (°C)	Structure	Crystallite size (nm)	Lattice parameters				E _g (eV)	E ₀
			<i>a</i> (Å)	<i>b</i> (Å)	<i>c</i> (Å)	<i>c/a</i>		
200	Hexagonal	45	10.5857	10.5857	14.9008	1.4076	3.15	0.1429
300	Hexagonal	48	10.5906	10.5906	14.8980	1.4067	3.13	0.1458
400	Hexagonal	48	10.5938	10.5938	14.8874	1.4052	3.17	0.1179
	Orthorhombic	43	3.9594	13.8515	3.6967	-	-	-
500	Orthorhombic	46	3.9626	13.8747	3.6979	-	3.20	0.0873

3.2 Thermal properties

Fig. 2 shows the thermogravimetric and differential thermal analyses of an as-prepared MoO₃ powder sample. The curve shows four obvious weight loss steps. From 50°C to 200°C, the first weight loss step is about 2.82%, corresponding to the removal of water adsorbed on the MoO₃ surface [23].

In the second stage from 200 to 450°C, the weight loss is about 2.77%, caused by the combustion of ammonium compounds from the MoO₃ powder sample [24, 25]. The third step in the temperature range 450-700°C slightly increased the sample mass by 0.36 % due to uptake of oxygen [26]. Finally, the fourth step of weight loss at temperatures above 700°C is attributed to the sublimation of MoO₃ [27]. Characterization with DTA is shown in Fig.2b. It was performed in order to study the phase transformations of MoO₃. An exothermic peak gave 432°C as the estimated phase transition temperature, from metastable h-MoO₃ to the thermodynamically stable α-MoO₃ structure [23]. This corroborates the phase transformation of MoO₃ inferred from the XRD patterns in Fig.1 because at high calcination temperatures, the increased mobility of atoms causes re-crystallization of MoO₃ that transforms the crystallite structure.

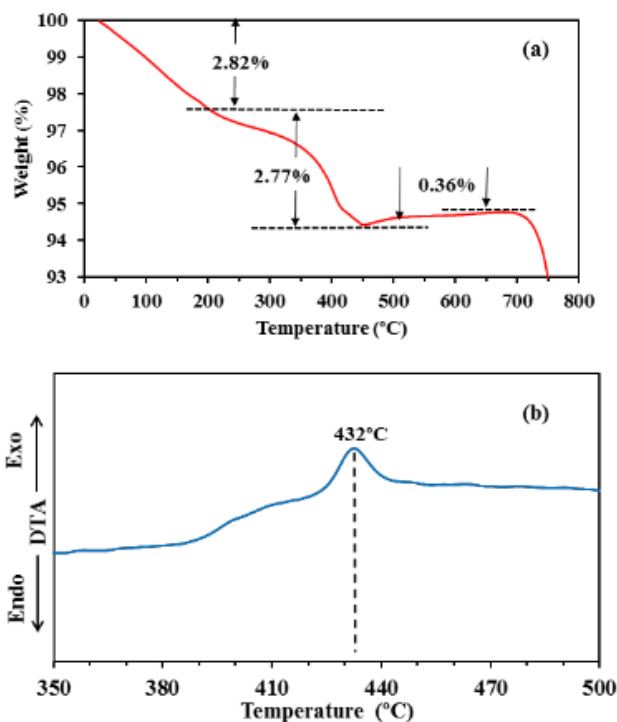


Fig.2 (a) TGA and (b) DTA curves of an as-prepared MoO_3 powder

3.3 Morphological studies

The morphologies of the nanocrystalline MoO_3 powder samples were assessed from SEM images. Fig.3(a, b) and 3(c) shows SEM micrographs of the aggregation of hexagonal rod particles, and growth from a center to form flower-like aggregates when calcined at 200 and 300°C. The diameter of each hexagonal rod is about 500 nm to 3 μm , and the length about 2 to 9 μm . This phenomenon is due to the minimization of surface energy [28]. For the MoO_3 powder calcined at 400°C, both hexagonal rods and hexagonal plates are clearly observed in Fig. 3(d). These hexagonal rods have diameters from 360 nm to about 2 μm , and lengths of about 2.6-7.3 μm . The diameters of the hexagonal plates, such as those marked by red dashed lines in Fig. 3(d), were about 1.4 to 4 μm with thicknesses of about 140 nm. When the calcination temperature was raised from 400°C to 500°C (Fig. 3(e) and Fig. 3(f)), the morphology changed from rods to plates, like those shown in Fig. 3(d). The diameter of MoO_3 platelets was in the range 3 to 8 μm , and the average thickness more than 140 nm. The decreasing length and diameter of the MoO_3 products with calcination temperature is attributed to the temperature promoting grain growth [21]. The size of the MoO_3 particles, which was measured from the SEM micrographs, was larger than the crystallite size calculated from Scherrer's equation, which indicated that the particles were polycrystalline.

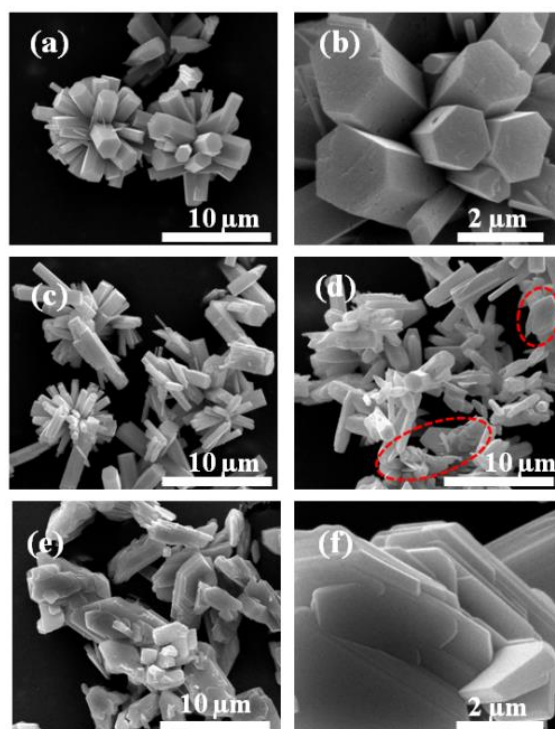


Fig. 3 SEM micrographs of nanocrystalline MoO_3 powder calcined at (a) (b) 200°C, (c) 300°C, (d) 400°C and (e) (f) 500°C

3.4 FT-IR analysis

The FT-IR spectra of the calcined nanocrystalline MoO_3 samples are given for the wavenumber range 4000-400 cm^{-1} in Fig.4. All the spectra show a broad absorption band at 3433, and a sharp band at 1607 cm^{-1} , which are attributed to stretching and bending vibrations of -OH in the water adsorbed on MoO_3 surfaces. The strengths of these bands decreased with the calcination temperature of nanocrystalline MoO_3 , matching results reported by M. Dhanasankar *et al.* [10].

A metal oxide generally provides absorption bands below 1000 cm^{-1} due to interatomic vibrations [3]. For h- MoO_3 calcined at 200-400°C such peaks are present at 919 and 977 cm^{-1} , indicating Mo=O [29]. The peak at 700 cm^{-1} is characteristic of Mo-O stretching and bending vibrations [30]. The peaks at around 527 and 576 cm^{-1} are due to Mo-O vibrations, in good agreement with reference [29].

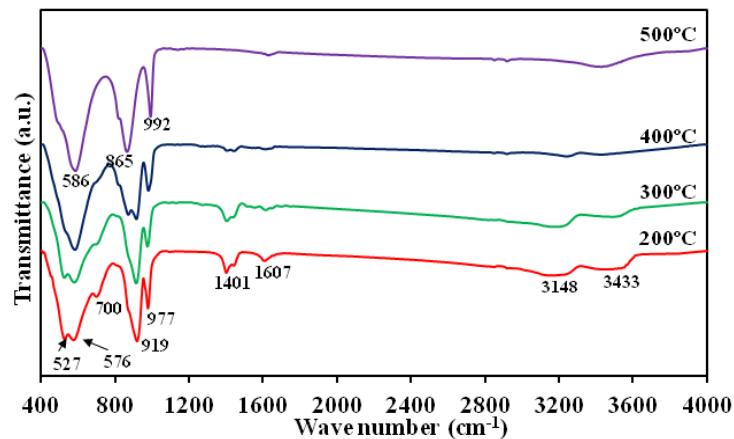


Fig.4 FT-IR spectra of nanocrystalline MoO_3 samples calcined at various temperatures.

The α - MoO_3 shows three major absorption peaks of metal oxide. Firstly, it is evident that the strong absorption band at 586 cm^{-1} is due to O-Mo-O stretching mode of corner-sharing oxygen atoms [30]. The second, oxygen stretching vibration mode of Mo-O-Mo occurs at 865 cm^{-1} with a strong absorption peak [29, 31]. The last major absorption peak of α - MoO_3 metal oxide is at 992 cm^{-1} , indicating Mo=O terminal stretching mode vibrations in the layered α - MoO_3 structure [29-31].

The broad absorption peak at 3148 and the sharp peak at 1401 cm^{-1} are assigned to the stretching and bending vibrations of N-H in NH_4^+ from residual AHM precursor[23], and the intensities of these bands decreased with calcination temperature. The N-H indications disappear with calcination at 500°C because the NH_4^+ from AHM decomposes above 450°C [24, 25], as also evidenced by the TGA/DTA analysis in Fig. 2.

3.5 XPS analysis

The oxidation state and chemical bonding state of nanocrystalline h- MoO_3 calcined at 300°C was further assessed by XPS analysis. The XPS results for Mo 3d, O 1s and C 1s are shown in Figs. 5(a), (b) and (c), respectively. The Mo 3d peaks were fit by two Gaussian curves, whose binding energies centered at 232.9 and 236.1 eV , relating to Mo 3d_{5/2} and Mo 3d_{3/2}, respectively. These two Mo 3d peaks confirm the oxidation state in MoO_3 as Mo^{6+} [32]. The binding energies of O 1s at 530.9 and 532.3 eV can be associated with the O^{2-} ion formation from MoO_3 [33], and with surface contamination such as C-O bonding [26], respectively. The last characteristic in these XPS spectra is the position of C 1s peak. The C 1s spectrum shown in Fig.5(c) can be decomposed into two peaks at 284.9 and 286.6 eV , indicating the $-\text{CH}_2-\text{CH}_2-$ and the C-O bonds of hydrocarbon contaminants adsorbed from air on the surface [34, 35], respectively.

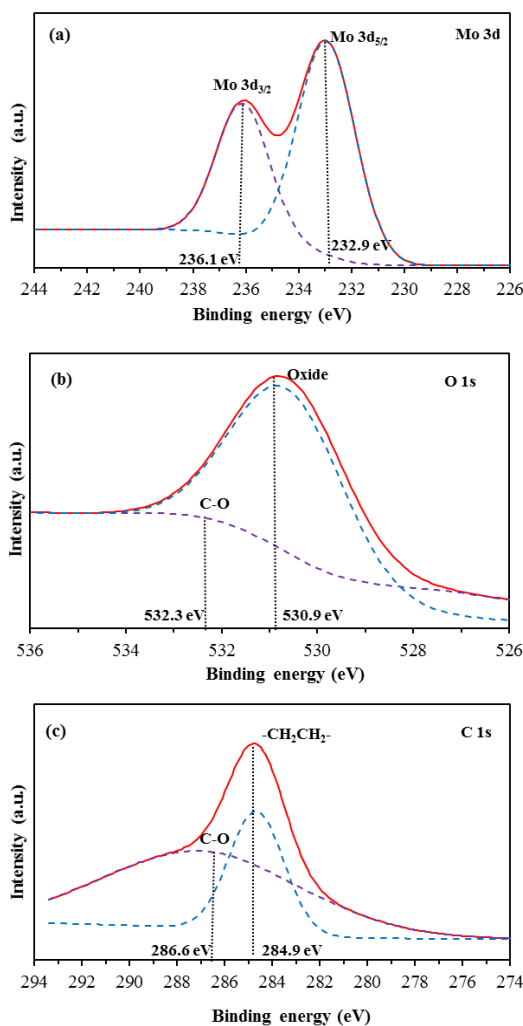


Fig.5 X-ray photoelectron spectra of nanocrystalline h- MoO_3 calcined at 300°C .

3.6 Optical properties

The UV–Vis DRS spectra of the nanocrystalline MoO_3 samples are shown in Fig.6. The absorbance spectra were measured for wavelengths in the range 350–550 nm. It is obvious that all samples were highly transparent in this visible spectral region. The absorption peak shifts towards longer wavelengths (red-shift) with the calcination temperature.

Based on the absorption spectra, we can calculate the band gap energy from [13, 36, 37]:

$$(\alpha E) = A'(E-E_g)^m \quad (7)$$

where A' is a constant, $E (= hc/\lambda)$ is the photon energy, E_g is the optical band gap, α is the optical absorption coefficient, and $m = 1/2$ for direct transition and $m = 2$ for indirect transition. The coefficient α can be approximated by [36]:

$$\alpha = A/d \quad (8)$$

where A is the measured absorbance and d is the thickness of the samples in a UV–vis cell (0.4 cm). Further, E can be approximated by:

$$E = 1,240/\lambda \quad (9)$$

where λ is the measured wavelength in nanometers.

The optical band gap energy of nanocrystalline MoO_3 is found by extrapolating the linear portion in an $(\alpha hv)^2$ vs. hv plot, as shown in Fig.7. The band gaps of nanocrystalline MoO_3 calcined at 200, 300, 400 and 500°C were about 3.15, 3.13, 3.17 and 3.20 eV, respectively. There was a clear increase in band gap energy with the highest calcination temperature, relative to the lower temperatures. The energy band gap of a material depends upon various factors, such as degree of crystallinity, structure otherwise, morphology, particle size distribution, and lattice defects [29, 34].

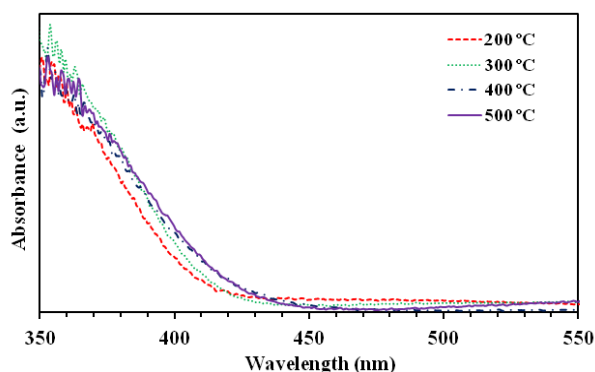


Fig.6 Optical spectra of nanocrystalline MoO_3 calcined at various temperatures.

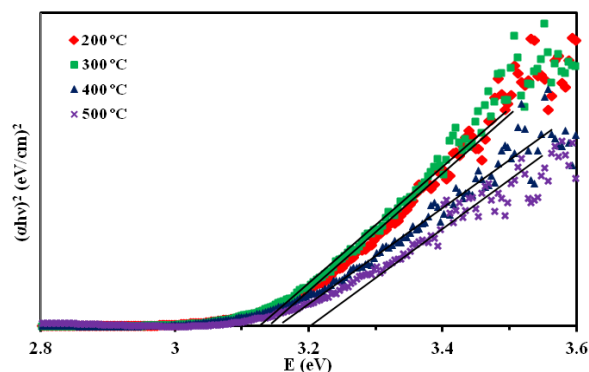


Fig.7 The $(\alpha hv)^2$ versus E curves of nanocrystalline MoO_3 samples calcined at various temperatures.

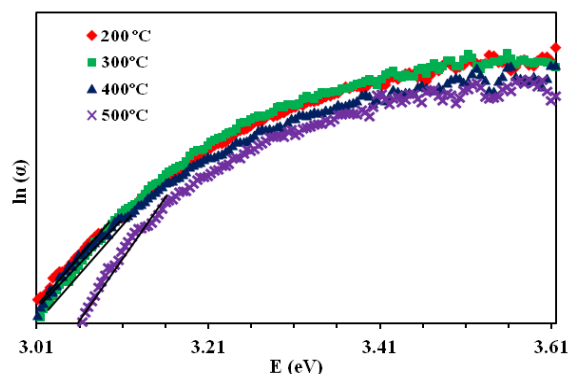


Fig.8 The $\ln(\alpha)$ versus E plots are used to estimate the defect concentrations in nanocrystalline MoO_3 powders calcined at various temperatures.

Moreover, the band gap energy also depends on the defect concentration. In this work, the decrease in the band gap energy value may be attributed to the occupation of electrons in oxygen vacancies that act as donor centers. The centers are in the forbidden gap and form a narrow donor band below the conduction band [12], giving rise to narrow band gap energy. The defect concentration can be estimated as follows [38,39]:

$$\alpha E = \alpha_0 \exp(E/E_0) \quad (10)$$

where α is the absorption coefficient estimated from the measured absorbance, α_0 is a constant, E is the photon energy and E_0 is an empirical parameter that depends on the defect concentration, temperature and structural disorder. Plots of the natural logarithm of α vs. E are shown in Fig. 8, and the reciprocal slopes imply E_0 estimates of the defect concentration as summarized in Table 1. When the calcination temperature increases the defect concentration of MoO_3 decreases, and the α - MoO_3 powder calcined at 500°C had the lowest defect concentration (oxygen vacancies). Relative to the h- MoO_3 powders calcined at 200 - 400°C it had red-shift in the band gap (higher band gap energy), increased grain size [21], decreased defect density in the tail states, and relaxation of distorted or dangling bonds [11].

3.7 Photochromic properties

Fig.9 shows the colour differences (ΔC) before and after UV irradiation for various times. For all nanocrystalline MoO_3 samples, the colour difference increased with UV irradiation time. The photochromic mechanism of MoO_3 is modeled by double insert/extraction of H^+ ion from water molecules adsorbed on MoO_3 surface and electrons, to form hydrogen molybdenum bronze ($\text{H}_x\text{Mo}^{\text{V}}_x\text{Mo}^{\text{VI}}_{1-x}\text{O}_3$) as follows [8, 40]:



The photochromic efficiency of h- MoO_3 calcined at 200 - 300°C was clearly better than that of α - MoO_3 calcined at 500°C . This observed difference in photochromic properties may be explained by differences in various factors.

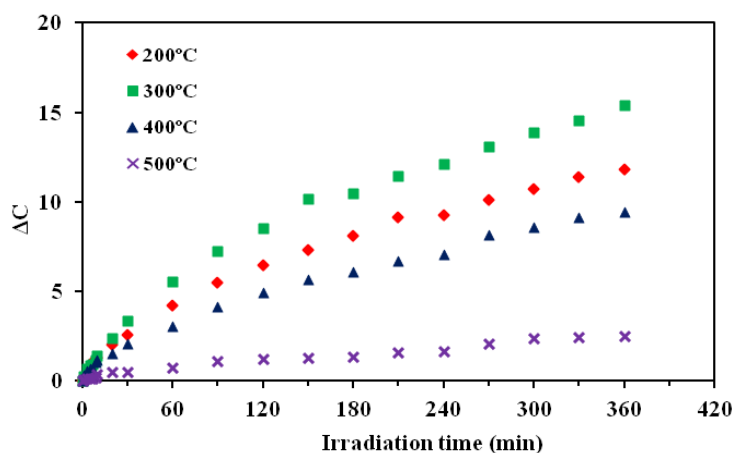


Fig.9 The colour differences (ΔC) as functions of UV irradiation time, for nanocrystalline MoO_3 powders calcined at various temperatures

Firstly, the h- MoO_3 had better photochromic properties than the α - MoO_3 matches the general notion that metastable structures often provide new and improved properties relative to thermodynamically stable structures [18]. The metastable h- MoO_3 that is composed of zigzag chains of MoO_6 octahedra connected at *cis*-positions acts as a tunnel structure. This hexagonal tunneling structure in metastable h- MoO_3 provides channels for H^+ , and the intercalation of monovalent ions facilitates electron-hole separation in the photochromic mechanism of Eq. (11). The trapped H^+ ions then form $\text{H}_x\text{Mo}^{\text{V}}_x\text{Mo}^{\text{VI}}_{1-x}\text{O}_3$, observed in the photochromic properties. Meanwhile, the thermodynamically stable orthorhombic MoO_3 (α - MoO_3) has an MoO_6 octahedral base in its unit cell, and all the MoO_3 components share edges and corners forming a zigzag chains and a layered structure, but the tunnel formation is missing from this structure [33].

Secondary, a low band gap energy promotes the formation of hydrogen molybdenum bronze. The defect concentration (oxygen vacancies) contributes to the diffusion of protons generated from the reaction of adsorbed water with holes (Eq.(12)), so these can easily diffuse into the MoO_3 lattice and combine with MoO_3 to form $\text{H}_x\text{Mo}^{\text{V}}_x\text{Mo}^{\text{VI}}_{1-x}\text{O}_3$ (Eq. (13)) and rapidly turns deep blue. A low band gap energy and a high defect concentrations in h- MoO_3 are probably the primary reasons for its higher photochromic efficiency relative to α - MoO_3 . This agrees well with the optical analysis in Fig.7 and Fig.8.

Finally, the amount of surface absorbed water on MoO_3 might have been important. The FT-IR results in Fig.4 show a lesser amount of -OH groups in the α - MoO_3 (calcined at 500°C) than in the h- MoO_3 (calcined at lower temperatures). This indicates that the moisture absorption on h- MoO_3 is higher than on α - MoO_3 , contributing to photochromic properties.

The photos in Fig.10 show nanocrystalline h- MoO_3 and α - MoO_3 powders before and after 360 minute UV irradiation. The h- MoO_3 powders (200°C and 300°C) are white and pale-blue in colour, changing to blue or deep blue with UV irradiation. In contrast, the α - MoO_3 (500°C) was pale-gray and turned to deep-gray with similar UV exposure. The MoO_3 calcined at 400°C was intermediate in nature, suggesting that initial white colour indicates h- MoO_3 while pale-gray indicates the α - MoO_3 , based on the XRD patterns in Fig.1. After 360 minute UV irradiation, the white h- MoO_3 powders distinctly turned deep-blue or pale purple, while the pale-gray α - MoO_3 changes less dramatically due to its lesser photochromic properties. This agrees well with the photochromic mechanisms discussed earlier.

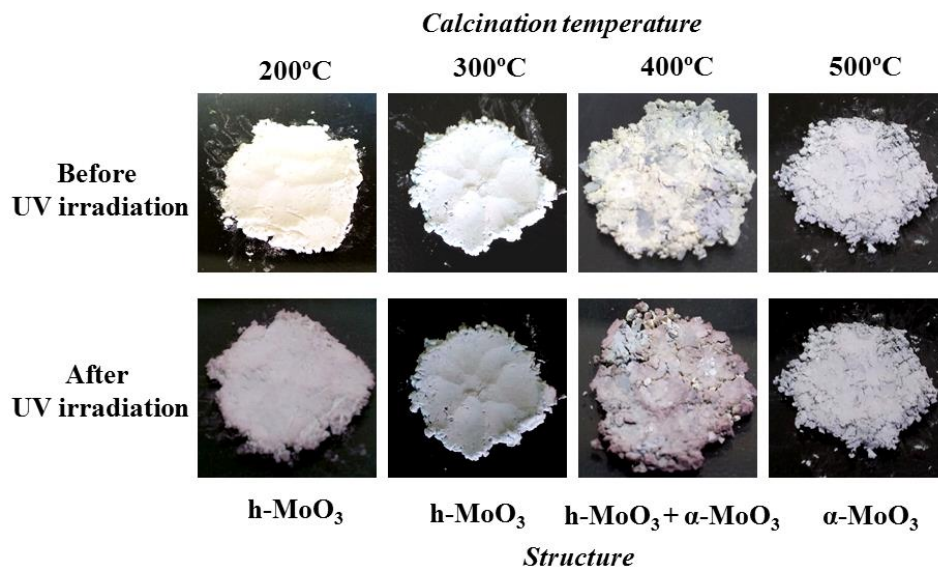


Fig.10 Photographic images of the nanocrystalline h-MoO₃ and α-MoO₃ powder samples calcined at different temperatures before and after exposure under UV irradiation for 360 min.

4. Conclusions

Nanocrystalline MoO₃ was successfully synthesized via precipitation, and hexagonal and orthorhombic structures were controllably created by calcination at various temperatures. The hexagonal flower-like MoO₃ transformed to orthorhombic microplate structured MoO₃ at high calcination temperatures, as confirmed by XRD; and by DTA. The phase transition temperature was determined to be 432°C. The photochromic performance of hexagonal MoO₃ was profoundly better than that of orthorhombic MoO₃.

Acknowledgments

Financial support from the Thailand Research Fund through the Royal Golden Jubilee Ph.D. Program and Prince of Songkla University (Grant No. PHD/0020/2554) is acknowledged. The authors also acknowledge the Department of Mining and Materials Engineering, Faculty of Engineering, Graduate school, Prince of Songkla University and Asst. Prof. Dr. Sumetha Suwanboon, Department of Materials Science and Technology, Faculty of Science, Prince of Songkla University. We thank the Synchrotron Light Research Institute (SLRI) of Thailand, Beamline 3.2a PES and Beamline 4.1 IR, for assistance in characterizations. We would like to thank Assoc. Prof. Dr. Seppo Karrila and Dr. Matthana Khangkhamano who provided helpful comments and suggestions on the manuscript.

References

- [1] G. Jin, W. Weng, Z. Lin, N.F. Dummer, S.H. Taylor, C.J. Kiely, J.K. Bartley, G.J Hutchings, *J. Catal.***296**, 55 (2012).
- [2] R. Pandeewari, B.G. Jeyaprakash, *Biosens. Bioelectron.***53**, 182(2014).
- [3] V.M. Mohan, H. Bin, W. Chen, *J. Solid State Electr.* **14**, 1769 (2010).
- [4] M. Kovendhan, D.P. Joseph, P. Manimuthu, S. Sambasivam, S.N. Karthick, K. Vijayarangamuthu, A. Sendikumar, K. Askan, H.J. Kim, B.C. Choi, C. Venkateswaran, R. Mohan, *Appl. Surf. Sci.***284**, 624 (2013).
- [5] C. Zollfrank, K. Gutbrod, P. Wechsler, J.P. Guggenbichler, *Mater. Sci. Eng. C***32**, 47 (2012).
- [6] S.A. Tomás, M.A. Arvizu, O. Zelaya-Angel, P. Rodriguez, *Thin Solid Films.***518**, 1332(2009).

- [7] M. Dhanasankar, K.K. Purushothaman, G. Muralidharan, *Solid State Sci.***12**, 246(2011).
- [8] Y. Shen, R. Huang, Y. Li, S. Yao, *Appl. Surf. Sci.***258**, 414(2011).
- [9] Z. Shen, G. Chen, Y. Yu, Q. Wang, C. Zhou, L. Hao, Y. Li, L. He, R. Mu, *J. Mater. Chem.***22**, 19646(2012).
- [10] M. Dhanasankar, K.K. Purushothaman, G. Muralidharan, *Appl. Surf. Sci.***257**, 2074(2011).
- [11] I. Navas, R. Vinodkumar, V.P.M. Pillai, *Appl. Phys. A.***103**, 373 (2011).
- [12] A. Bouzidi, N. Benramdane, H. Tabet-Derraz, C.Mathieu, B. Khelifa, R. Desfeux, *Mater. Sci. Eng. B.***97**, 5(2003).
- [13] Y.J. Lee, C.W. Park, D.G. Kim, W.T. Nichols, S.T. Oh, Y.D. Kim, *J. Ceram. Process. Res.***11**, 52(2010).
- [14] J. Song, X. Ni, L. Gao, H. Zheng, *Mater. Chem. Phys.***102**, 245 (2007).
- [15] G.G. Allogho, P.V. Ashrit, *Thin Silid Films.***520**, 2326 (2012).
- [16] A.D. Sayede, T. Amriou, M. Pernisek, B. Khelifa, C. Mathieu, *Chem. Phys.***316**, 72(2005).
- [17] R. Irmawati, M. Shafizah, *Int. J. Basic Appl. Sci.***09**, 34 (2009).
- [18] O. Mougin, J. Dubois, F. Mathieu, A. Rousset, *J.Solid State Chem.***152**, 353 (2000).
- [19] K. Srinivasa Rao, K.V. Madhuri, S. Uthanna, O.M. Hussain, C. Julien, *Mater. Sci. Eng. B.***100**, 79(2003).
- [20] J.N. Yao, Y.A. Yang, B.H. Loo, *J. Phys. Chem. B.***102**, 1856 (1998).
- [21] A.Gaber, M.A. Abdel-Rahim, A.Y. Abdel-Latif, M.N. Abdel-Salam, *Int. J. Electrochem. Sci.***9**, 81 (2014).
- [22] R.W. Kelsall, I.W. Hamley, M. Geoghegan, *Nanoscale Science and Technology*, John Wiley and Sons, West Sussex (2005).
- [23] A. Chithambararaj, A.C. Bose, *Beilstein J. Nanotechnol.***2**, 585 (2011).
- [24] R.S. Mann, K.C. Khulbe, *B. Chem. Soc. Jpn.***48**, 1021 (1975).
- [25] K. Manukyan, D. Davtyan, J. Bossert, S. Kharatyan, *Chem. Eng. J.***168**, 925(2011).
- [26] S. Bai, S. Chen, L. Chen, K. Zhang, R. Luo, D. Li, C.C. Liu, *Sensors Actuat. B- Chem.***174**, 51(2012).
- [27] R.F. de Farias, *J. Phys. Chem. Solids.***64**, 1241(2003).
- [28] R.L. Penn, J.F. Banfield, *Geochim. Cosmochim. Ac.* **63**, 1549(1999).
- [29] P. Wongkrua, T. Thongtem, S. Thongtem, *J. Nanomater.***2013**, 1 (2013).
- [30] T.H. Chiang, H.C. Yeh, *J. Alloy. Compd.***585**, 535 (2014).
- [31] A. Klinbumrung, T. Thongtem, S. Thongtem, *J. Nanomater.***2012**, 1 (2012).
- [32] L. Zheng, Y. Xu, D. Jin, Y. Xie, *Chem. Mater.***21**, 5681 (2009).
- [33] Z. Li, L. Gao, S. Zheng, *Mater. Lett.***57**, 4605 (2003).
- [34] G.E. Buono-Core, G. Cabello, A.H. Klahn, A. Lucero, M.V. Nuñez, B. Torrejón, C. Castillo, *Polyhedron.***29**, 1551(2010).
- [35] J. Wlatowska-Mrowlecka, S.D. Diesbach, V. Maurice, S. Zanna, L. Klein, E. Briand, I. Vickridge, P. Marcus, *J. Phys. Chem. C.***112**, 11050 (2008).
- [36] S. Suwanboon, P. Amornpitoksuk, A. Sukolrat, *Ceram. Int.***37**, 1359 (2011).
- [37] Z. Hussain, *J. Mater. Res.***16**, 2695 (2001).
- [38] P. Jittiarporn, L. Sikong, K. Kooptarnond, W. Taweepreda, *Ceram. Int.***40**, 13487 (2014).
- [39] P. Jitti-a-porn, S. Suwanboon, P. Amornpitoksuk, O. Patarapaiboolchai, *J. Ceram. Process. Res.***12**, 85 (2011).
- [40] Y. Shen, R. Huang, Y. Cao, P. Wang, *Mater. Sci. Eng. B.***172**, 237 (2010).